Additive manufacturing of high-strength crack-free Ni-based Hastelloy X superalloy

Quanquan Han[a,b*], Yuchen Gu[c], Rossitza Setchi[b*], Franck Lacan[b], Richard Johnston[c], Sam L. Evans[b], Shoufeng Yang[d*]

[a]Centre for Advanced Jet Engineering Technologies (CaJET), Key Laboratory of High Efficiency and Clean Mechanical Manufacture, Centre for Additive Manufacturing, School of Mechanical Engineering, Shandong University, Jinan 250061, China

[b]Cardiff School of Engineering, Cardiff University, Cardiff, CF24 3AA, UK

[c]College of Engineering, Swansea University, Swansea, SA1 8EN, UK

[d]Department of Mechanical Engineering, KU Leuven, Celestijnenlaan 300B, box 2420, Heverlee B-3001, Leuven, Belgium

Corresponding authors:

Quanquan Han: Hanq1@cardiff.ac.uk, Hanquanquan@sdu.edu.cn, +4402920876266

Rossitza Setchi: Setchi@cardiff.ac.uk, +4402920875720

Shoufeng Yang: Shoufeng.yang@kuleuven.be, +3216324999

Abstract

Laser powder bed fusion (LPBF) is a proven additive manufacturing (AM) technology for producing metallic components with complex shapes using layer-by-layer manufacture principle. However, the fabrication of crack-free high-performance Ni-based superalloys such as Hastelloy X (HX) using LPBF technology remains a challenge because of these materials' susceptibility to hot cracking. This paper addresses the above problem by proposing a novel method of introducing 1 wt.% titanium carbide (TiC) nanoparticles. The findings reveal that the addition of TiC nanoparticles results in the elimination of microcracks in the LPBF-fabricated enhanced HX samples; i.e. the 0.65% microcracks that were formed in the as-fabricated original HX were eliminated in the as-fabricated enhanced HX, despite the 0.14% residual pores formed. It also contributes to a 21.8% increase in low-angle grain boundaries (LAGBs) and a 98 MPa increase in yield strength. The study revealed that segregated carbides were unable to trigger hot cracking without sufficient thermal residual stresses; the significantly increased subgrains and low-angle grain boundaries played a key role in the hot cracking elimination. These findings offer a new perspective on the elimination of hot cracking of nickel-based superalloys and other industrially relevant crack-susceptible alloys. The findings also

have significant implications for the design of new alloys, particularly for high-temperature industrial applications.

Keywords: Powder bed fusion; nickel-based superalloy; Hastelloy X; cracking; nanoparticle

1. Introduction

Laser powder bed fusion (LPBF) is an advanced technology for additive manufacturing (AM) in which metallic powder is selectively melted layer by layer using a high-power laser [1][2][3]. This technology offers the ability to fabricate complex parts for a range of strategic sectors, including aerospace, automotive and medical devices [4][5][6][7]. Nickel-based superalloys such as Hastelloy X (HX) exhibit an extraordinary combination of oxidation resistance, formability, and mechanical properties in the temperature range of 540–1000°C. For these reasons, such materials are widely applied in gas turbine engine components [8][9][10]. However, due to the significant temperature gradient and the rapid cooling rate of up to 10^6 K/s when processed by LPBF process [11], nickel-based superalloys are prone to hot cracking, which degrades their mechanical and physical properties. Also, the large thermal gradient in the molten pool prevents nucleation ahead of the solidification front, which then leads to residual thermal stress accumulation, epitaxial columnar grains, and the formation of cracks across several pre-solidified layers [12].

The alloying elements that are specifically included to improve both the mechanical and thermal properties of nickel-based superalloys contribute to their susceptibility to hot cracking. For instance, although Mo and Cr contribute to the carbides formation, which helps to control grain size and increases resistance to grain boundary sliding at elevated temperatures [13], these two alloying elements make nickel-based superalloys more susceptible to hot cracking, which is triggered by the combination of sufficient thermal stresses and a liquid film [14][15]. The reduction of micro-cracking can be achieved by modifying the chemical composition of HX. For example, the reduction of Mn and Si content contributes to an increase of the tensile strength at high temperature (1033 K) without discernible increase at room temperature [11]. The composition modification method, however, is unable to eliminate all microcracks within the LPBF of HX alloy. Post-treatments such as hot isostatic pressing (HIP) are commonly used to eliminate microcracks and improve

the strength-ductility trade-off of the as-fabricated parts [16][17]. It has been reported that commercially available HX powders supplied by two original equipment manufacturers, SLM Solutions and EOS, were also prone to hot cracking when processed by LPBF [18][19][20]. Moreover, it was suggested in [18] that HIP processing is an effective approach to eliminate such microcracks. Although HIP processing is capable of closing microcracks and improving the fatigue performance of LPBF-fabricated HX parts [16], such processing does result in excessive grain growth and coarsening [21]. In addition, the cost of the extra post-processing reduces the economic attractiveness of metal LPBF. Therefore, this type of post-treatment hence does not represent an ideal alternative in order to mitigate hot cracking defects and limit their effect on the mechanical behaviour of nickel-based superalloys [22][23][24]. Sanchez-Mata et al. [25] investigated the microstructure of LPBF-fabricated HX, and cracks were not observed under their optical microscopy examination, however the detailed process parameters that were employed were not disclosed.

This paper proposes and validates a novel method to eliminate hot cracking defects by introducing TiC nanoparticles and promoting the heterogeneous nucleation during the LPBF of HX parts. A similar approach previously reported how the addition of zirconium nanoparticles to high-strength aluminium alloys promotes fine-grain formation, which allows strength comparable to wrought materials [26]. TiC ceramic particles have been previously utilised in the laser AM of Inconel 625 superalloys as a reinforcement to improve the tensile strength and wear performance. The TiC particles were selected in [27] [28] because of their extremely high hardness, high thermal dynamic stability in nickel matrix and a low friction coefficient. Moreover, the particle size of the TiC ultrafine disperse in [27] [28] was in the range of 5 to 7 µm. In contrast, the size of the TiC nanoparticles employed in this study is less than 200 nm and the TiC was determined by calculating the lattice disregistry between potential catalysts and nickel (the matrix in HX) on the basis of both Turnbull-Vonnegut and planar crystallographic disregistry theories [29][30]; the nanoparticles are uniformly dispersed using a high-speed mixing technique at room temperature.

2. Experimental methods

2.1. High-speed powder mixing

The commercial gas atomised Hastelloy X (HX) powder used in this work was from LPW Technology Ltd (Widnes, UK), with an alloying composition (wt.%) of 21.2Cr–17.6Fe–8.8Mo–2Co–0.06C–0.6W–0.2Si–0.1Mn–bal.Ni. Titanium carbide (TiC) nanoparticles (< 200 nm, TEM) were acquired from Sigma Aldrich (UK). A Malvern Mastersizer 3000 (Malvern, UK) equipment was used to determine the particle size distribution (PSD) of both HX and TiC powders. A commercial high-speed mixer (SpeedMixer, DAC 800.1 FVZ, Hauschild, Germany) with a maximum mixing speed of 2,000 rpm was employed to synthesise the HX-1wt.% TiC feedstock (enhanced HX); the mixer allows to blend 300g powder at once at room temperature. The mixing parameters employed included a 1,200 rpm mixing speed with a total of 5 minutes of mixing time; to prevent overheating, the mixing procedure was to mix for 2.5 minutes, pause for 5 minutes, and then mix again for 2.5 minutes.

2.2. Laser powder bed fusion (LPBF)

A Renishaw AM250 (Renishaw Plc, UK) which is equipped with a modulated ytterbium fibre laser (wavelength = 1071 nm) was used in this study to fabricate the cubic (8 x 8 x 8 mm^3) and tensile specimens. The substrate was not preheated before the build. The tensile specimens were fabricated horizontally where the loading direction is perpendicular to the build direction, and their shape and dimensions were determined based on ASTM-E8/E8M-13a [31] (as shown in the tensile performance section). Although the horizontally manufactured specimens exhibit higher tensile strength compared to the vertically fabricated parts [32][33], the vertical manufacture scenario however costs much more metal powder to fill the build volume. Also, the formation and spatial distribution of the microcracks was independent upon the build scenario in LPBF of HX alloy [17]; the horizontal manufacture scenario was thus used in the present study. The optimised LPBF process parameters were determined by examining the relative density of the manufactured cubic samples. Both the original and enhanced HX were found to have the same optimum LPBF process parameters to manufacture the cubic samples. The optimum primary parameters employed in this study are: laser power = 200 W, exposure time = 100 µs (equivalent to 600 mm/s scanning speed), layer thickness = 40 µm, hatch spacing = 120 µm, rotation angle = 67°, scanning strategy = chessboard.

2.3. Materials characterisation

Both original and enhanced HX samples were vertically sectioned (parallel to the build direction), ground, and then polished (3 µm, 1 µm diamond suspension, and OPS colloidal silica, 0.04 µm) using standard techniques before scanning electron microscopy (SEM) and optical microscopy (OM) inspections [34]. Please be advised that all specimens were examined in the as-fabricated condition without any post-processing treatments. In order to reveal the rapid solidification structures and molten pool boundaries, the polished cubic specimens were subjected to electrochemical etching for 10 s in oxalic acid; the samples for backscattered electron (BSE) SEM and electron backscatter diffraction (EBSD) analysis were only polished, without chemical etching. High-resolution BSE imaging and electron backscatter diffraction (EBSD) scanning were performed using a JEOL 7800F high-resolution field emission gun scanning electron microscope (FEG-SEM) equipped with a Nordlys EBSD detector and an Aztec analysis system (Oxford Instruments).

The EBSD scanning was operated under 20 kV and performed on an area of 1×1 mm^2 with a step size of 0.8 µm. The post-data processing was completed using the HKL-EBSD Channel 5 software package. The interfaces between grains were classified as low-angle grain boundaries (LAGBs) when the misorientation angle was between 2° and 10°; otherwise, the angles were regarded as high-angle grain boundaries (HAGBs). X-ray microtomography scanning, which was conducted to spatially investigate the size and distribution of defects (e.g. microcracks and micropores), was performed on a lab-based Zeiss Xradia Versa 520 (Carl Zeiss XRM, Pleasanton, CA, USA) X-ray microscope using a CCD detector system with scintillator-coupled visible light optics and a tungsten transmission target. Identical X-ray settings were used for the scanning of both specimens. An X-ray tube voltage of 140 kV and a tube current of 72 µA were used, with an exposure of 4,000 ms and a total of 3,201 projections. An objective lens that yielded an optical magnification of four was selected with binning set to two, which produced isotropic voxel (3-D pixel) sizes of 2.8623–2.8631 µm.

To optimise attenuation and contrast, a 1.6 mm copper filter was placed between the source and specimen. The slices produced by the XMReconstructor were imported into Avizo software (ThermoFisher Scientific, Waltham, MA, USA), where a

digital region of interest of 1.43 mm x 1.43 mm x 1.43 mm was selected within both samples to focus on the internal material for the analysis. Post-processing, including reorientation, noise reduction, binarisation, and segmentation, allowed the extraction of pores and cracks from the Hastelloy material. Image threshold was applied to determine the defect content (%) at each 2-D slice using ImageJ software. Transmission electron microscopy (TEM) observations were performed on an FEI Titan Themis 80-300 equipped with two aberration correctors and a highly efficient (four-quadrant) energy-dispersive X-ray system.

2.4. Mechanical characterisation

The uniaxial tensile tests were performed using a computer-controlled Zwick/Roell tester (maximum load of 100 kN) with a strain rate of 1.33×10^{-3} s^{-1} at room temperature. The obtained engineering stress-strain curves were derived from two specimens for both conditions (original and enhanced HX materials).

3. Results and discussion

3.1. Enhanced Hastelloy X feedstock for LPBF

The enhanced feedstock consists of 99 wt.% commercial HX (Fig. 1a–c) and 1 wt.% TiC nanoparticles. This novel HX feedstock was synthesised using a high-speed mixing technique, and the TiC nanoparticles were found to be uniformly distributed among the original HX powder. In contrast, the initial TiC nanoparticles were observed to significantly agglomerate due to the high surface energy with an average size of 4.41 µm, while the original HX was measured to have an average size of 31.2 µm (Fig. 1c). The methodology was validated during feedstock synthesis by an inspection of the sieved particles. The TiC nanoparticles were evenly attached to the HX after sieving (Fig. 1e), which confirmed that the high-speed mixing technique could be used to coat properly the TiC nanoparticles without settling.

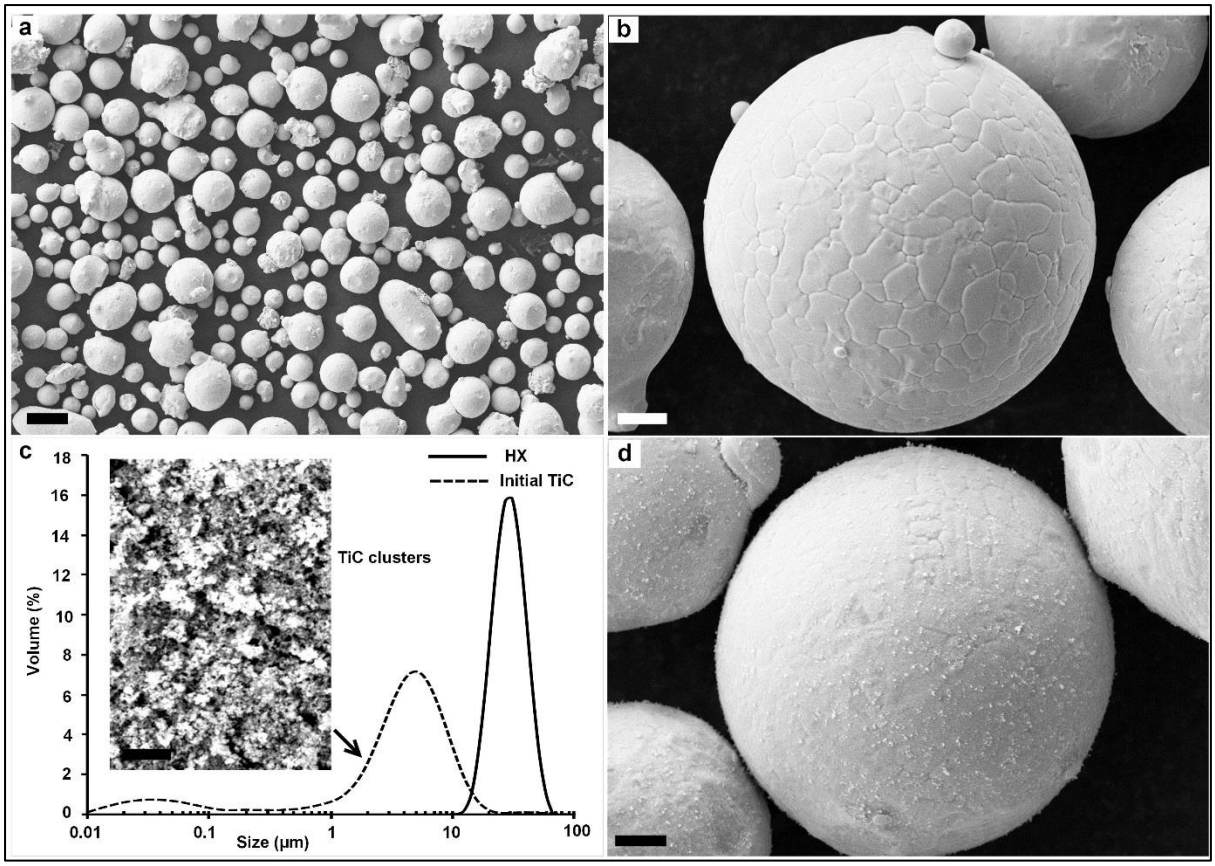

Fig. 1. Original and enhanced nanoparticle-coated Hastelloy X (HX) powder for laser powder bed fusion (LPBF). **a** A scanning electron microscopy (SEM) image of original commercial HX powder. **b** A high-magnification SEM image of original HX powder, revealing spherical particle morphology and the grain boundaries. **c** A SEM image showing TiC clusters and particle size of original HX with Dv (50) of 31.2 μm and initial TiC particles with Dv (50) of 4.41 μm analysed using laser diffraction; **d** High magnification SEM image of TiC nanoparticle coated HX, revealing a fairly uniform distribution of TiC after sieving. Scale bars are 40 μm for **a**, 5 μm for **b** and **d**, 2 μm for **c.**

TiC nanoparticles were selected in this study because the TiC lattice structure exhibits a smaller planar crystallographic disregistry with a nickel (Ni) lattice structure compared to other widely used nucleating agents such as WC, Zr, ZrC, and SiC lattice structures. The crystallographic disregistry was first proposed by Turnbull and Vonnegut and afterwards improved from the linear to the planar scale by Bramfitt [29],[30]. The modified planar disregistry (δ) can be expressed as:

$$\delta_{(hkl)_n}^{(hkl)_s} = \sum_{i=1}^{3}\left(\frac{\left|d[uvw]_s^i cos\theta - d[uvw]_n^i\right|}{3 \cdot d[uvw]_n^i}\right) \qquad (1)$$

where $(hkl)_s$ and $(hkl)_n$ are the low-index crystallographic planes of TiC and nickel in this study, respectively, and $[uvw]_s$ and $[uvw]_n$ denote the low-index directions in the $(hkl)_s$ and $(hkl)_n$ planes, respectively. The $d[uvw]_s$ and $d[uvw]_n$ values represent the interatomic spacing along $[uvw]_s$ and $[uvw]_n$, respectively, while θ denotes the angle between the $[uvw]_s$ and $[uvw]_n$. When the low-index

crystallographic planes $(100)_{TiC}$, $(100)_{Ni}$, $(110)_{Ni}$, and $(111)_{Ni}$ were used, the planar crystallographic disregistry was determined to be 20.9% between TiC and nickel; both materials had a face-centre cubic (FCC) crystal structure (Fig. 2 and Table 1).

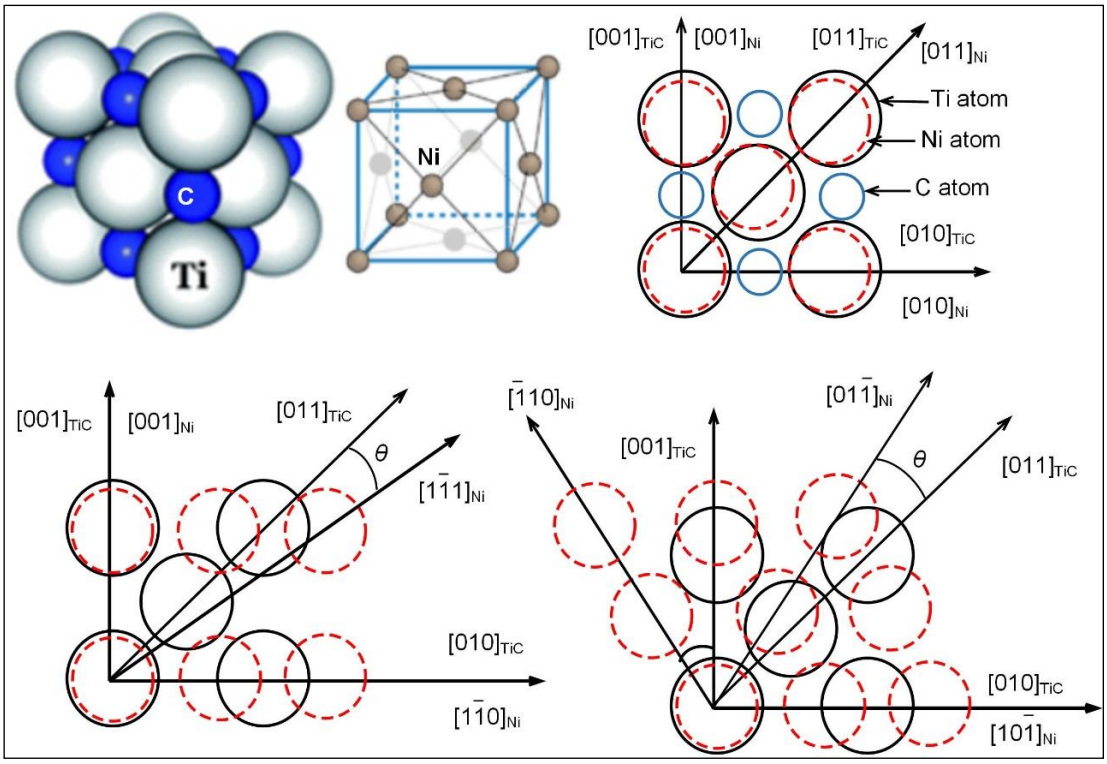

Fig. 2. Schematic representation of lattice disregistry between the face centre cubic (FCC) Ni and TiC crystal structures. This representation is based on Turnbull-Vonnegut and planar crystallographic disregistry theories.

Table 1.

Planar disregistry between titanium carbide and nickel.

Case	$[uvw]_s$	$[uvw]_n$	$d[uvw]_s$	$d[uvw]_n$	θ, deg	δ
$(100)_{TiC}$ || $(100)_{Ni}$	$[010]_{TiC}$	$[010]_{Ni}$	4.375	3.62	0	20.9%
	$[011]_{TiC}$	$[011]_{Ni}$	3.09	2.56	0	
	$[001]_{TiC}$	$[001]_{Ni}$	4.375	3.62	0	
$(100)_{TiC}$ || $(110)_{Ni}$	$[010]_{TiC}$	$[1\bar{1}0]_{Ni}$	4.375	2.56	0	31.1%
	$[011]_{TiC}$	$[1\bar{1}1]_{Ni}$	3.09	6.27	9.73	
	$[001]_{TiC}$	$[001]_{Ni}$	4.375	3.62	0	
$(100)_{TiC}$ || $(111)_{Ni}$	$[010]_{TiC}$	$[10\bar{1}]_{Ni}$	4.375	2.56	0	44.5%
	$[011]_{TiC}$	$[01\bar{1}]_{Ni}$	3.09	2.56	15	
	$[001]_{TiC}$	$[\bar{1}10]_{Ni}$	4.375	2.56	30	

3.2. Microstructure and microcrack elimination mechanism

The formation of microcracks in LPBF-manufactured HX samples is mainly attributable to two factors. First, the alloying composition, particularly the carbon element (0.06 wt.% in the HX powder used for this study); under the rapid heating in LPBF, the segregated carbide phases are unable to fully dissolve into the surrounding matrix so that partial dissolution occurs which forms a low melting point eutectic liquid film at the grain boundary region. Second, the accumulated thermal residual stresses within the sample pull on the liquid film on the grain boundary and lead to the formation of microcracks, which is similar to the findings in [14]. This suggests that hot cracking can only occur when the two factors are combined; since the alloying composition of HX cannot be changed in this study, reducing the distributed thermal stress on grain boundaries would be an effective method to address the hot cracking issue in LPBF of HX alloys. It has been known [35][36] that increasing the low-angle grain boundaries (LAGBs) such as the increase in dislocations is capable of strengthening the grain boundary cohesion and uniforming the distribution of strain that is induced by thermal stress; the dislocation induced stress may also counteract the accumulated residual stresses. The TiC crystal exhibits a relatively small planar crystallographic disregistry (20.9%) with FCC nickel crystal. The addition of TiC nanoparticles is thus expected to function as a nucleating agent to promote heterogeneous nucleation and contribute to an increase in LAGBs.

Microstructure characterisation of both as-fabricated samples revealed a two-dimensional (2D) distribution of microcracks and pores (Fig. 3a/d). The microcracks were found to be the primary defect for the original HX; their length varied from several microns to more than 100 microns. A few residual pores were detected in the enhanced HX, but no microcracks have been observed in the enhanced HX sample under OM inspection. Fig. 3b/e show the molten pools and defects that were formed in both samples. In addition to the microcracks observed, several molten pools were found to exhibit larger dimensions (e.g. a molten pool depth) than the rest of the pools in the original HX, while the enhanced HX exhibited fairly uniform and consistent molten pools. This could be explained by the fact that the uniformly coated TiC nanoparticles altered the material's thermal conductivity and regulated the laser absorption. Both columnar dendritic and cellular fine structures were formed in the as-fabricated original and enhanced samples (Fig. 3c/f). This confirms previous studies with other metals and alloys, which have reported that LPBF

contributes to fine microstructure formation [37][38][39]. The SEM images show agreement with the OM observations that the microcracks in the original HX exhibit random distribution and are propagated along the build direction. Microcracks have not been observed in the enhanced HX under both OM and SEM inspections, suggesting that the added TiC nanoparticles resulted in the hot cracking elimination.

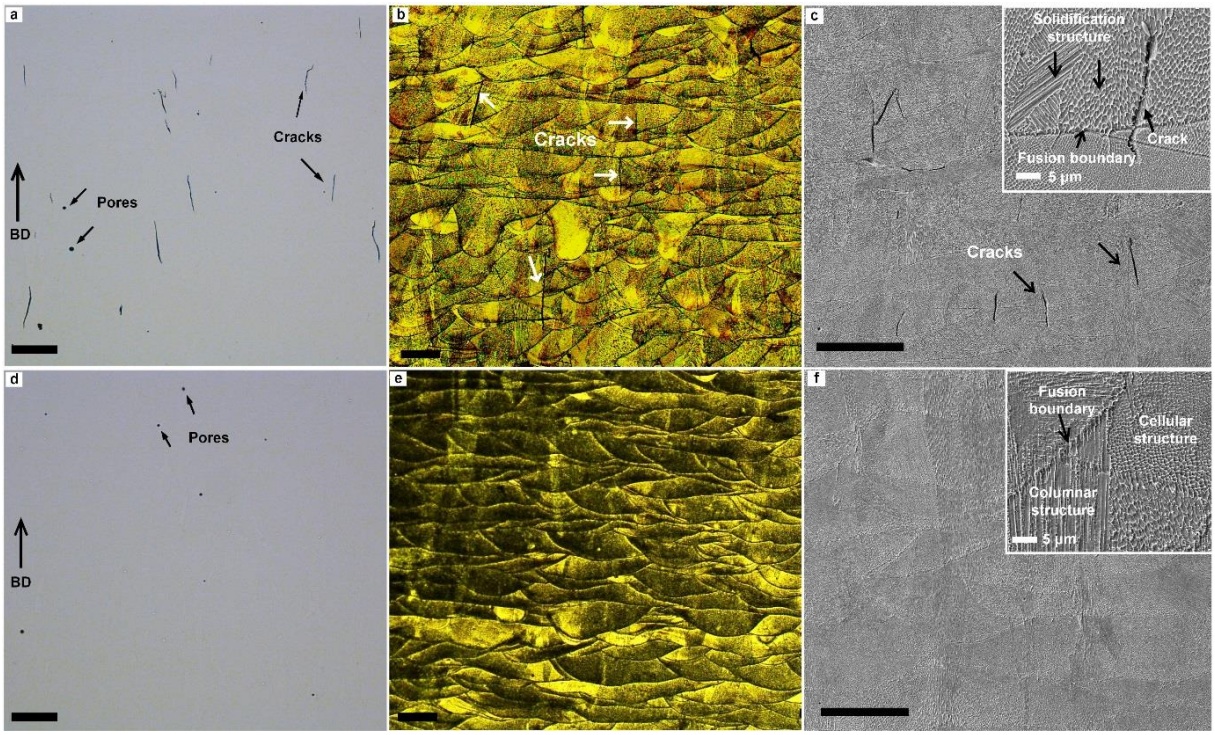

Fig. 3. Defects and microstructure of original and enhanced HX. **a** An optical microscopy (OM) image showing microcracks and pores in original HX. **b** An OM image of the chemically etched original HX, revealing the molten pools, cracks and fusion boundaries. **c** A SEM image of etched original HX, revealing the columnar and cellular solidification structures. **d** An OM image of enhanced HX, revealing a limited number of observed pores. **e** Uniform molten pools and fusion boundaries in the enhanced HX. **f** A SEM image showing the very fine solidification structures in enhanced HX. Scale bars are100 μm.

The high-resolution X-ray microtomography (X-ray CT) measurements further revealed the spatial distribution of microcracks and pores in both samples (1.43 x 1.43 x 1.43 mm^3). The reconstructed three-dimensional (3D) defects from both top and side views (Fig. 4a–b) showed that the microcracks were uniformly formed and distributed in the as-fabricated HX, while only a few pores were detected in the enhanced HX (Fig. 4c). The formation of residual pores (also known as open pores [40] [41]) could be caused by insufficient wettability of molten pool to TiC nanoparticles; at the very last solidification stage, pores formed at the interface between the matrix phase and TiC nanoparticles. Fig. 4d, which is a coupled image of Fig. 4a and c, shows the effect of TiC nanoparticles on microcrack elimination.

ImageJ used to determine defect density (%) with respect to the 2-D slice number offers a statistic support for the microcracks elimination in the enhanced HX (Fig. 4e). The 2-D greyscale slices from the high-resolution CT measurements revealed that the crack density in original HX varied from 0.34% to 0.99% with an average density of 0.65% in the obtained 500 slices, while the residual pore density in the enhanced HX was determined to range from 0.038% to 0.41% with an average value of 0.14%. The typical defect density images from both original (slice No. 150) and enhanced HX (slice No. 210) are also shown in Fig. 4e. Based on the CT examination, the microcracks that formed in original HX exhibit an average length of 97.2 μm and thickness of 95.6 μm, while the average residual pore size in the enhanced HX was measured to be 18.9 μm without cracks detected (Fig. 4f).

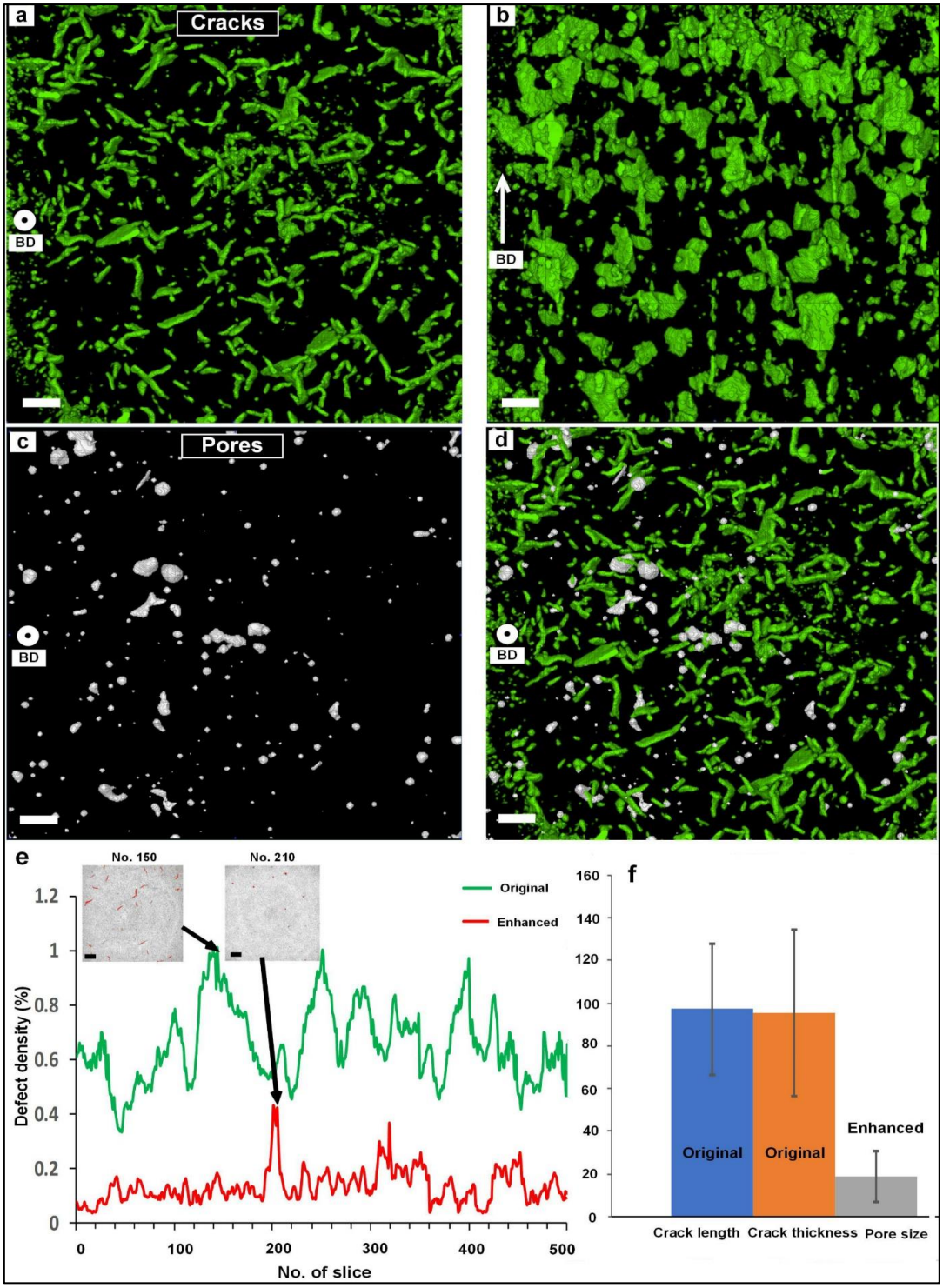

Fig. 4. X-ray microtomography measured and Avizo reconstructed defects. **a** Top view of the Avizo reconstructed defects for original HX, revealing that most of the defects are microcracks. **b** Side view of the reconstructed defects for original HX. **c** Top view of the reconstructed defects for enhanced HX, revealing most of the defects are residual pores. **d** Top view of the coupled defects from original (green) and enhanced (grey) HX samples. **e** ImageJ calculated defect density (%) with respect to the slice number for both cases. **f** Comparison of defect size between original and enhanced samples. Scale bars are100 μm.

Further microstructure characterisation revealed intergranular microcracks in the as-fabricated HX (Fig. 5). The as-fabricated HX exhibited a typical LPBF-generated

heterogeneous microstructure [37][42][43][44], where epitaxial columnar grains had formed along the build direction (Fig. 5a, b). It should be noted that because the fine columnar grains had grown epitaxially to the build layers, the grains had an orientation relationship and so appear larger than their true size in the electron backscatter diffraction (EBSD) image (Fig. 5c). Interestingly, the microcracks were found to be distributed along the high-angle grain boundaries, or HAGBs (those >10º), which suggests that the microcracks that had formed were intergranular rather than transgranular cracks. This finding is consistent with the findings of a previous study on a non-weldable nickel superalloy using selective electron beam melting [14]. The backscattered electron (BSE) imaging in the present study confirmed during EBSD measurement that hot cracking had always occurred along the HAGBs (Fig. 5d).

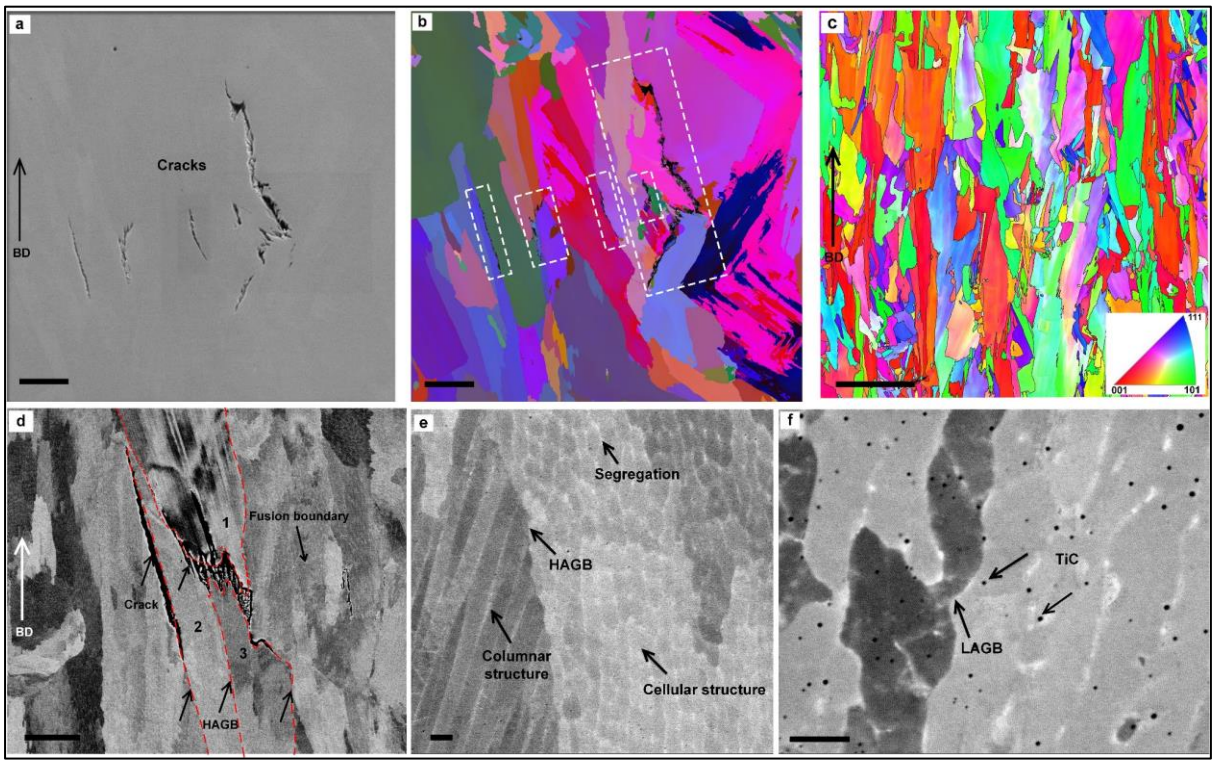

Fig. 5. Typical microstructure of as-fabricated original and enhanced HX samples. **a** Cross-sectional SEM image showing microcracks formed in original HX. **b** Electron backscatter diffraction (EBSD) Euler map of the sample in **a**, showing the microcracks along high-angle grain boundaries (HAGBs, >10º). **c** EBSD inverse-pole figure (IPF) map of the original HX, revealing the columnar grains. **d** Backscattered electron (BSE)-SEM image showing the intergranular microcracks in the original HX. **e** A high-magnification BSE-SEM image of the original HX, showing columnar and cellular solidification structures as well as the alloying elements segregation to the solidification walls. **f** A high magnification BSE-SEM image of enhanced HX, revealing a uniform distribution of TiC nanoparticles among austenite matrix. Scale bars are 25 μm for **a** and **b**; 200 μm for **c**;10 μm for **d** and 1 μm for **e** and **f**.

High-resolution BSE imaging was used to show the chemical segregation to solidification walls and grain boundaries in both original and enhanced samples (Fig. 5e/f). Although carbide segregation is believed to contribute to hot cracking, such cracking was not found in our enhanced HX (Fig. 5f), which suggests that the added TiC nanoparticles influenced the grain boundaries' physical properties at the solidification stage, thus eliminating the hot cracks. Indeed, TiC nanoparticles were observed to be uniformly distributed in the *Y-FCC* austenite matrix after the solidification. The average size of the observed TiC nanoparticles was measured to be 61.8 nm using ImageJ software. It should be noted that these nanoparticles exhibited relatively spherical morphology and existed separately in the matrix, implying the Marangoni force that was induced by surface tension tended to separate the nanoparticle clusters rather than further agglomerating them at the liquid-solid phase transformation stage.

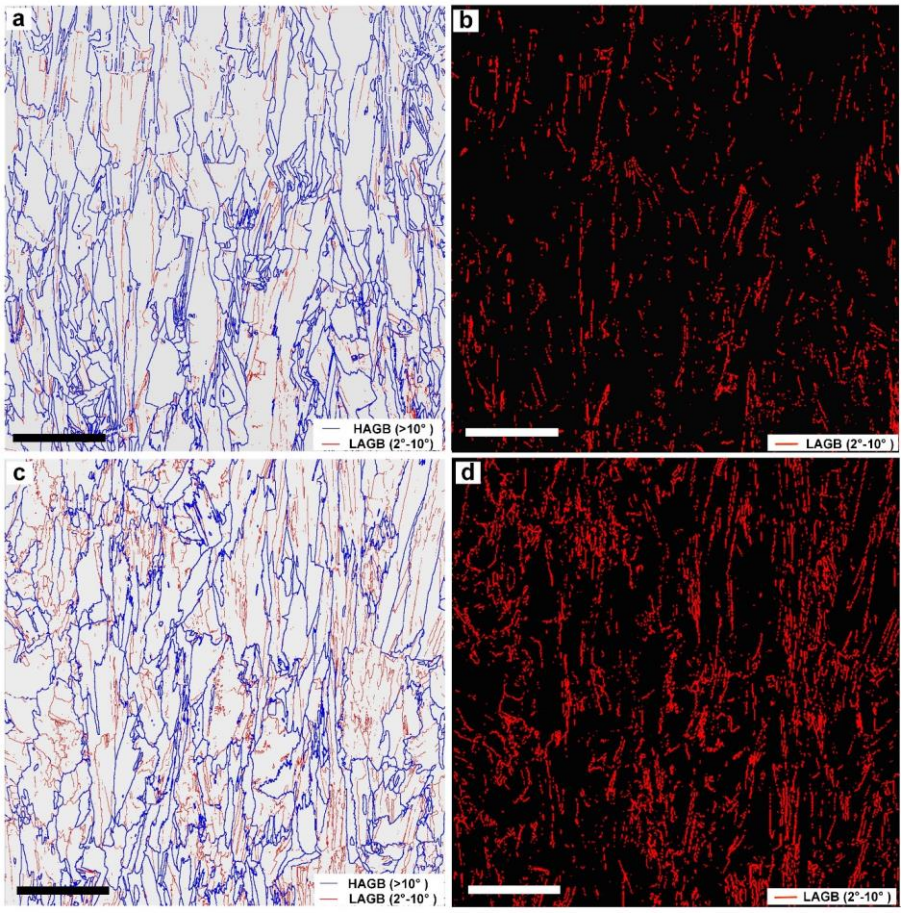

Fig. 6. EBSD images of as-fabricated original and enhanced HX samples. **a** EBSD image quality (IQ) map with HAGBs and low-angle grain boundaries (LAGBs) superimposed for the original HX. As indicated in the legend, HAGBs (>10º) are coloured blue and LAGBs (2º-10º) are red. **b** Extracted LAGBs from **a**; the fraction of LAGBs is 26.4%. **c** EBSD IQ map for enhanced HX. **d** Extracted LAGBs from **c**; the fraction of LAGBs is 48.2%. Scale bars are 200 μm for **a**–**d**.

Fig. 6 shows the EBSD image quality (IQ) maps with HAGBs and low-angle grain boundaries (LAGBs) superimposed for original and enhanced HX, respectively. Epitaxial columnar grains were also observed in the enhanced HX, based on the EBSD measurements (Fig. 6c). Interestingly, the original and enhanced HX samples exhibited a significant difference in LAGBs: the fraction of LAGBs was determined to be 26.4% in the original HX (Fig. 6b), while the fraction value increased to 48.2% in the enhanced HX (Fig. 6d). This implies that the added TiC nanoparticles promoted heterogeneous nucleation at the liquid-solid phase transformation stage (i.e. solidification). The significantly increased LAGBs could be the primary contributor in the elimination of hot cracks in the as-fabricated enhanced HX.

Further transmission electron microscopy (TEM) and energy dispersive spectroscopy (EDS) studies revealed the hot cracking elimination mechanisms in the LPBF of HX. Columnar solidification structures with walls were observed in the original HX under bright-field TEM imaging (Fig. 7a); the columnar walls were not always parallel to the build direction. The size, orientation, and wall thickness of the fine solidification structures are known to be connected to solidification conditions (e.g. cooling rate, thermal gradient, or solidification front velocity) during the LPBF process [45][46][47]. The wall thickness was measured to be less than 120 nm in the original HX. High-angle annular dark-field (HAADF) scanning TEM (STEM) was used to show the elements' segregation to the columnar wall (Fig. 7b), while the EDS spectrum (Fig. 7c) taken from the columnar wall revealed the chemical composition to be 2.3 wt.% C, 5.83 wt.% O, 24.53 wt.% Cr, 2.55 wt.% Mn, 15.07 wt.% Fe, 2.23 wt.% Co, 33.87 wt.% Ni, and 13.58 wt.% Mo. Fairly weak Mg and Al peaks were also found to be present. The EDS analysis of the chemical composition of the raw powder material revealed that the segregations at the solidification walls were Mo-rich and Cr-rich carbides.

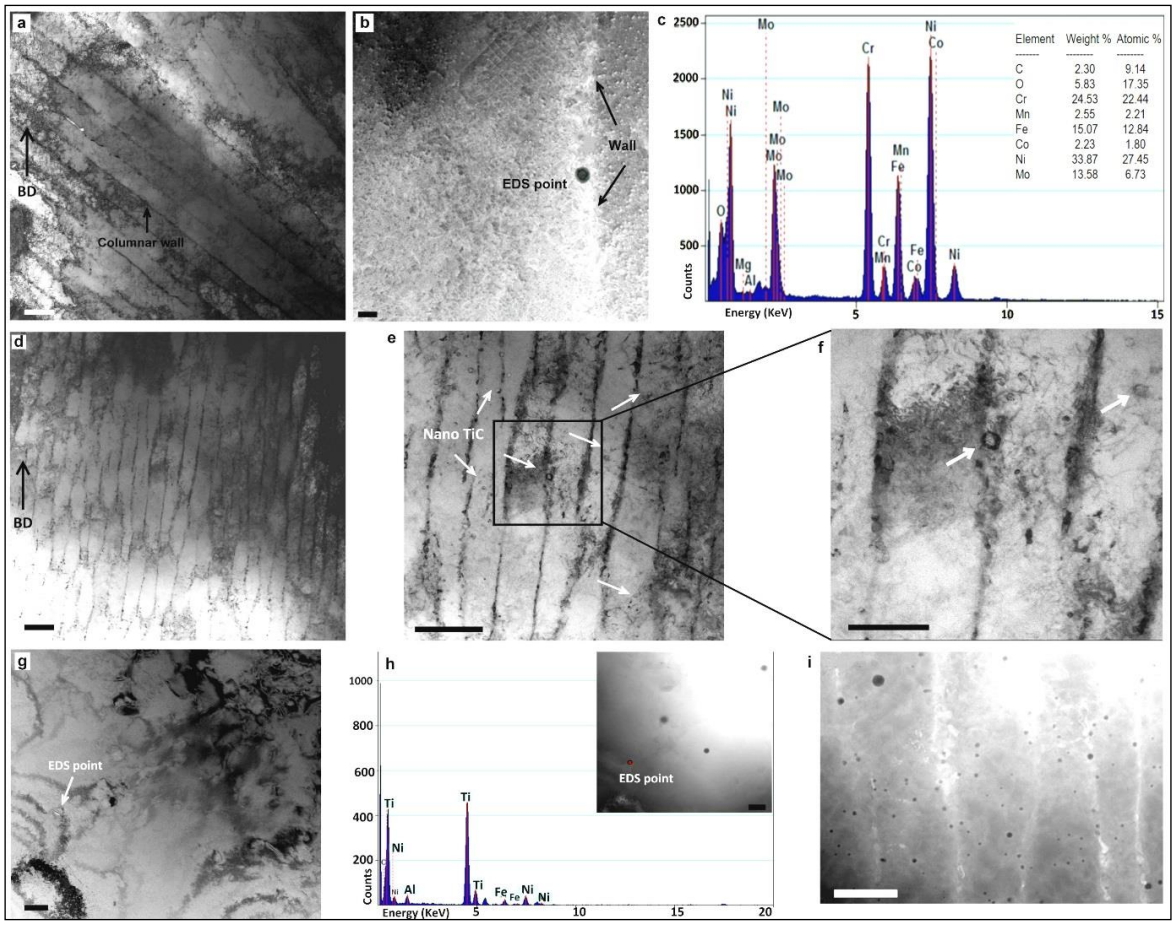

Fig. 7. Transmission electron microscopy (TEM) and energy dispersive spectroscopy (EDS) characterisations of original and enhanced HX samples. **a** A bright-field TEM image of original HX from vertical section, revealing the columnar solidification structures in original HX. **b** A high-angle annular dark-field (HAADF) scanning TEM (STEM) image of the solidification columnar wall in original HX. **c** EDS spectrum taken from the measure point shown in **b**. **d-f** bright-field TEM images of enhanced HX with different magnifications. **g** A TEM image of enhanced HX nanocomposite with observed TiC nanoparticle. **h** EDS spectrum taken from the measure point shown in **g**. **i** HAADF STEM image of enhanced HX, revealing the TiC nanoparticles and solidification walls. Scale bars are 1 μm for **a, d** and **e**; 100 nm for **b, g** and **h** and 500 nm for **f** and **i**

Fig. 7d-f show the bright-field TEM images of the enhanced HX, where several uniformly distributed nanoparticles were observed. The formed columnar walls were separated by the segregations to exhibit cellular-like structures, which were not observed in the original HX (Fig. 7a/d). Fig. 7h reveals the EDS spectrum taken from a measure point shown in Fig. 7g, where nanoparticles were observed. The detected strong Ti peaks indicate the existence of TiC nanoparticles in the fabricated enhanced HX. Fig. 8a shows the EDS characterisations of the enhanced HX taken from the measure area shown in Fig. 7i. Compositional mapping revealed Mo-rich and Cr-rich carbides along the walls of the solidification structures without any microcracks observed. In contrast, Fig. 8b shows the EDS maps of a typical microcrack zone from the original HX, where the segregated Mo and Cr rich carbides

were detected along the crack, implying that carbide segregation at the grain boundaries is one of the primary contributors for hot cracking. The EDS maps (Fig. 8a) also confirm that the added TiC nanoparticles were uniformly distributed in the matrix following solidification. Chemical reactions between TiC and other alloying elements were not found to have occurred in the enhanced HX as expected.

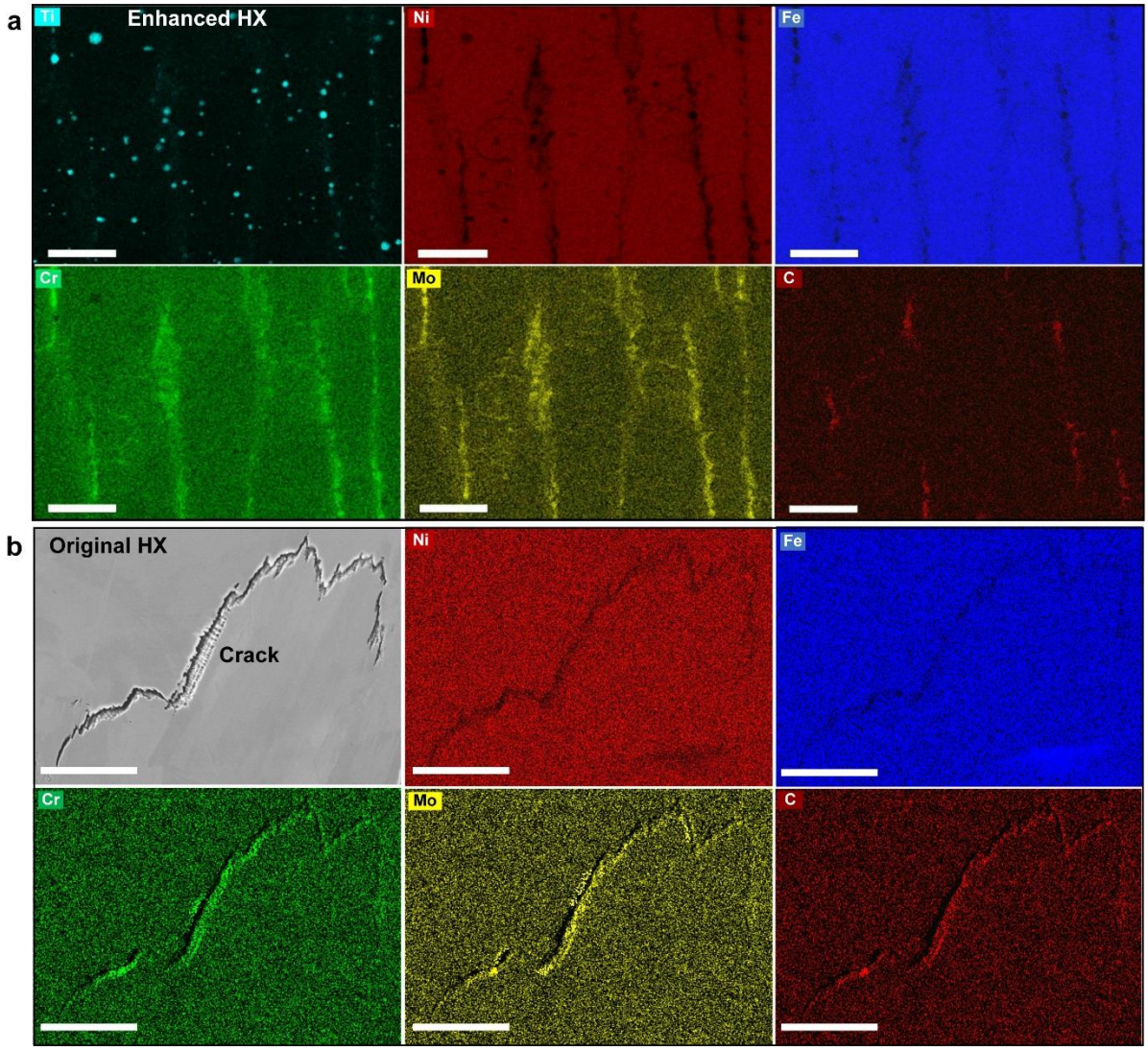

Fig. 8. Compositional mapping of the enhanced HX samples and original HX at the crack zone. **a** EDS maps showing the segregation of Mo and Cr rich carbides to the solidification walls in enhanced HX (from Fig. 7i). **b** Segregated Mo and Cr rich carbides on the microcrack in original HX. Scale bars: 500 nm for **a** and 25 µm for **b.**

When comparing the microstructure of both original and enhanced HX samples, one can see that segregated carbides had formed in both samples while the microcracks were only detected in the original HX, which exhibited much less number of LAGBs compared to the enhanced HX. This suggests that the significantly increased LAGBs in the enhanced HX must have played a key role in the elimination

of hot cracking. Indeed, a larger number of subgrains were observed in the enhanced HX (Fig. 9d-f) compared to the original HX (Fig. 9a-c). LAGBs were observed in both samples, but they were found to be surrounded by a higher density of dislocations in the enhanced HX. This higher density contributed to the formation of numerous equiaxed subgrains under 500 nm in size, which were much smaller than the subgrains within the original HX. As discussed before, the dislocations induced stress could counteract the thermal residual stresses and the LAGBs are capable of strengthening grain boundary cohesion because the feeding of the remaining molten material is always easier at the grain boundaries compared to the interdendritic areas. Also, the LAGBS could make a more uniform distribution of the strain induced by thermal stress. The hot cracking was thus eliminated, even though the segregation took place in the enhanced HX. This finding is also consistent with previous studies, which have suggested that an increase in LAGBs contributes to hot tearing resistance in the casting of nickel-based superalloys [35][36].

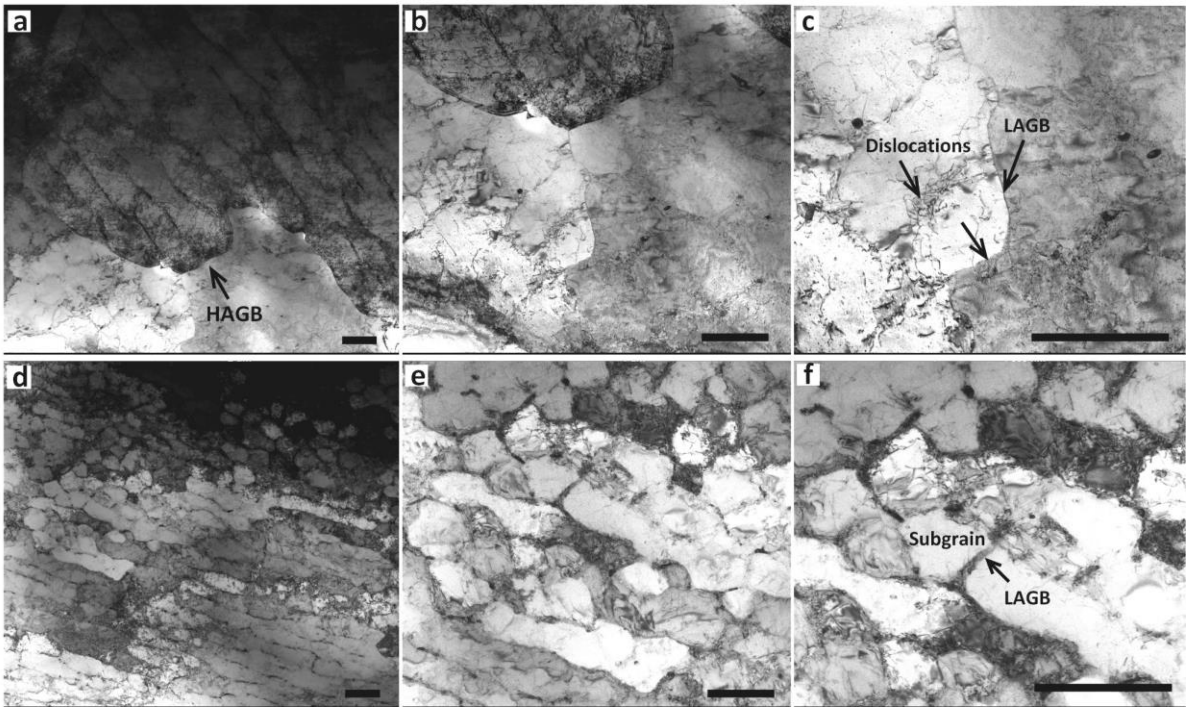

Fig. 9. Bright-field TEM images of original and enhanced HX samples. **a-c** TEM images of original HX under different magnifications. **d-f** TEM images of enhanced HX sample, showing a larger number of dislocations and LAGBs. Scale bars are 1 μm.

3.3. Tensile performance of HX

The tensile performances of both the original and enhanced HX samples were measured using uniaxial tensile testing at room temperature. The tensile behaviours

of the two enhanced HX specimens were examined to be consistent, with a 682 ± 5.6 MPa yield strength, 849 ± 1 MPa ultimate tensile strength, and 15 ± 4.2% elongation (Fig. 10a). The dimensions of the tensile samples based on the ASTM standards are also shown in Fig. 10a. Compared to the enhanced HX, the original HX exhibited about 98 MPa and 115 MPa lower yield strength and ultimate tensile strength, respectively. This increased performance can be attributed to the elimination of microcracks and the increase in grain boundaries that were induced by the TiC nanoparticles addition. The original HX specimens exhibited 19 ± 2.8% elongation, which was slightly higher than the enhanced HX (15 ± 4.2%), revealing that the added 1 wt.% TiC nanoparticles slightly degraded the ductility of this superalloy. In addition to the dimple structures, we also observed a large number of elongated and open cracks in the original HX's fracture surface (Fig. 10b), while only a very limited number of open pores were detected in the enhanced HX's fracture surface (Fig. 10c).

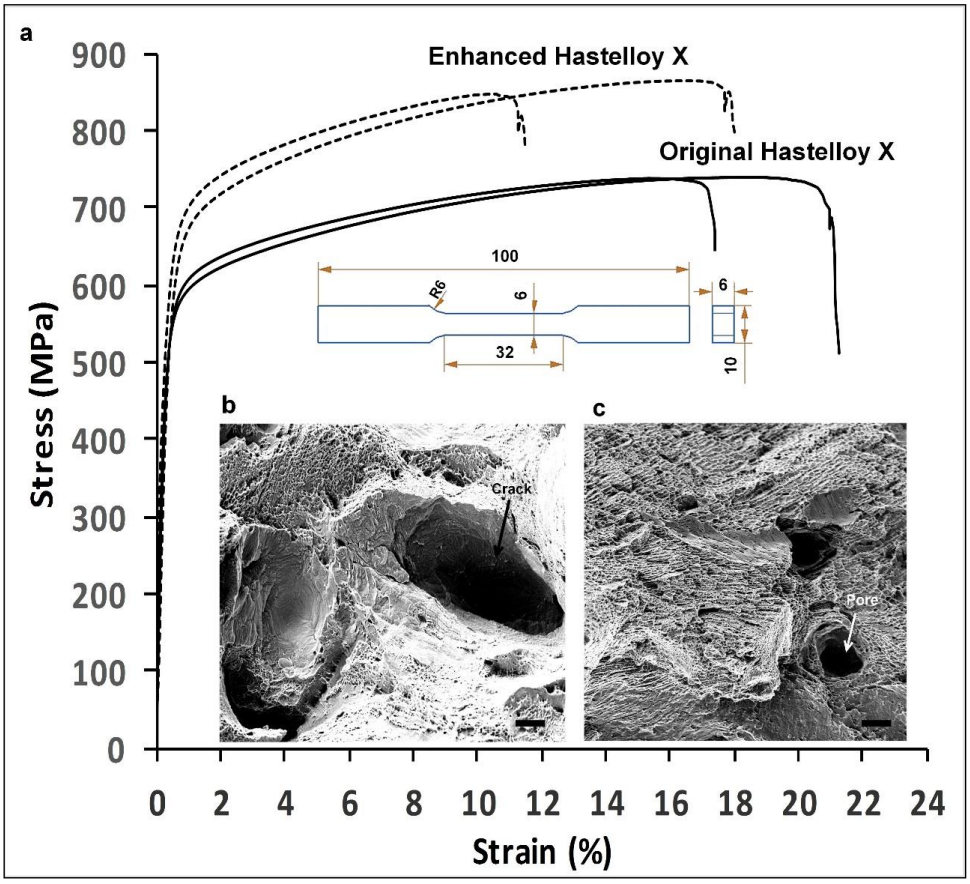

Fig. 10. Uniaxial tensile testing of as-fabricated HX. **a** Engineering stress-strain curves of original HX and enhanced HX nanocomposite. **b** SEM image of the original HX fracture surface, revealing the dimple structure and open cracks. **c** SEM image of enhanced HX fracture surface, showing dimple structure and pores. Scale bars are 5 μm for **b–c**

The added 1 wt.% TiC nanoparticles contributed to about 100 MPa tensile strength increase at room temperature. The reinforced nanoparticles that existed at the grain boundaries may function as the pinning points to hinder the dislocation movement to improve the tensile, creep and corrosion behaviours at elevated temperatures. Also, the added TiC nanoparticles were found to be able to eliminate the microcracks, which generally are the stress concentration sites where cracks initiate in both the low and high cycle fatigue testing. The enhanced HX material is expected to exhibit significant improvement in fatigue performance compared to the original HX, which will be investigated in future work.

4. Conclusions

The results obtained in this research reveal a novel path to eliminating microcracks during the LPBF of Hastelloy X by the addition of titanium carbide nanoparticles. Various factors of this setup were investigated, including hot cracking elimination mechanism, microstructure evolution, and mechanical properties. The following conclusions may be drawn from this study:

(1) The titanium carbide was adopted to manufacture Hastelloy X using LPBF because this material in general exhibits a small planar crystallographic disregistry (20.9%) with a nickel lattice structure. The high-speed powder mixing technique was proven to be an efficient method to disperse the titanium carbide nanoparticles uniformly among the Hastelloy X powder at room temperature and without settling.

(2) The quantified results confirm that the microcracks have been eliminated in the enhanced Hastelloy X due to the addition of 1 wt.% titanium carbide nanoparticles. That is, the 0.65% microcracks in LPBF-fabricated original Hastelloy X were eliminated in the fabricated enhanced HX despite the 0.14% of residual pores formed. The formed microcracks in original Hastelloy X were examined to have an average length of 97.2 μm and thickness of 95.6 μm, respectively, while the pore size in enhanced Hastelloy X was measured to be about 18.9 μm.

(3) The elimination of hot cracking in our enhanced Hastelloy X was achieved because the 1 wt.% titanium carbide nanoparticles resulted in a 21.8% increase in low-angle grain boundaries. The significantly increased grain

boundaries were believed to strengthen the boundaries' cohesion and make the accumulated thermal stresses uniform. The addition of titanium carbide nanoparticles also contributed to a 98 MPa increase in yield strength. Our study has also revealed that segregated carbides were unable to trigger hot cracking without sufficient thermal residual stresses.

These findings suggest a promising pathway to control liquid-solid and solid-solid phase transformations. The proposed nanoparticle-dispersion technique can also be applied to the synthesis of a wide range of metal matrix nanocomposites, making them suitable for crack-free processing using LPBF. To the best of our knowledge, the finding of this hot cracking elimination path for Hastelloy X opens an efficient pathway to eliminate microcracking in the AM of nickel-based superalloys and other industrially relevant crack-susceptible alloys. Our approach provides a positive impact in accelerating the AM of nickel-based superalloys for aerospace and other applications. This metallurgical approach also offers practical insights into the design of new alloy systems, particularly for metal-based AM processes.

Acknowledgements

This research was conducted within the framework of ASTUTE 2020, a joint collaborative project of Cardiff University and Swansea University.

References

[1] N. Guo, M.C. Leu, Additive manufacturing: Technology, applications and research needs, Front. Mech. Eng. 8 (2013) 215–243. doi:10.1007/s11465-013-0248-8.

[2] Q. Han, R. Setchi, F. Lacan, D. Gu, S.L. Evans, Selective laser melting of advanced Al-Al2O3 nanocomposites: Simulation, microstructure and mechanical properties, Mater. Sci. Eng. A. 698 (2017) 162–173. doi:10.1016/j.msea.2017.05.061.

[3] M. Rombouts, J.P. Kruth, L. Froyen, P. Mercelis, Fundamentals of selective laser melting of alloyed steel powders, CIRP Ann. - Manuf. Technol. (2006). doi:10.1016/S0007-8506(07)60395-3.

[4] Q. Han, H. Gu, S. Soe, R. Setchi, F. Lacan, J. Hill, Manufacturability of AlSi10Mg overhang structures fabricated by laser powder bed fusion, Mater. Des. 160 (2018) 1080–1095. doi:10.1016/j.matdes.2018.10.043.

[5] F. Martina, J. Mehnen, S.W. Williams, P. Colegrove, F. Wang, Investigation of the benefits of plasma deposition for the additive layer manufacture of Ti-6Al-4V, J. Mater. Process. Technol. 212 (2012) 1377–1386. doi:10.1016/j.jmatprotec.2012.02.002.

[6] P. Heinl, L. Müller, C. Körner, R.F. Singer, F.A. Müller, Cellular Ti-6Al-4V structures with interconnected macro porosity for bone implants fabricated by selective electron beam melting, Acta Biomater. 4 (2008) 1536–1544. doi:10.1016/j.actbio.2008.03.013.

[7] Q. Han, Y. Geng, R. Setchi, F. Lacan, D. Gu, S.L. Evans, Macro and nanoscale wear behaviour of Al-Al2O3 nanocomposites fabricated by selective laser melting, Compos. Part B

Eng. 127 (2017) 26–35. doi:10.1016/j.compositesb.2017.06.026.

[8] M.M. Attallah, R. Jennings, X. Wang, L.N. Carter, Additive manufacturing of Ni-based superalloys: The outstanding issues, MRS Bull. 41 (2016) 758–764. doi:10.1557/mrs.2016.211.

[9] J.C. Zhao, M. Larsen, V. Ravikumar, Phase precipitation and time-temperature-transformation diagram of Hastelloy X, Mater. Sci. Eng. A. 293 (2000) 112–119. doi:10.1016/S0921-5093(00)01049-2.

[10] Q. Han, H. Gu, R. Setchi, Discrete element simulation of powder layer thickness in laser additive manufacturing, Powder Technol. 352 (2019) 91–102. doi:10.1016/j.powtec.2019.04.057.

[11] N.J. Harrison, I. Todd, K. Mumtaz, Reduction of micro-cracking in nickel superalloys processed by Selective Laser Melting: A fundamental alloy design approach, Acta Mater. 94 (2015) 59–68. doi:10.1016/j.actamat.2015.04.035.

[12] A.A. Antonysamy, J. Meyer, P.B. Prangnell, Effect of build geometry on the β-grain structure and texture in additive manufacture of Ti6Al4V by selective electron beam melting, Mater. Charact. 84 (2013) 153–168. doi:10.1016/j.matchar.2013.07.012.

[13] M. Durand-Charre, The Microstructure of Superalloys, Gordon and Breach Science Publishers, Amsterdam, 1997.

[14] E. Chauvet, P. Kontis, E.A. Jägle, B. Gault, D. Raabe, C. Tassin, J.J. Blandin, R. Dendievel, B. Vayre, S. Abed, G. Martin, Hot cracking mechanism affecting a non-weldable Ni-based superalloy produced by selective electron Beam Melting, Acta Mater. 142 (2018) 82–94. doi:10.1016/j.actamat.2017.09.047.

[15] G. Marchese, G. Basile, E. Bassini, A. Aversa, M. Lombardi, D. Ugues, P. Fino, S. Biamino, Study of the microstructure and cracking mechanisms of hastelloy X produced by laser powder bed fusion, Materials (Basel). 11 (2018) 106. doi:10.3390/ma11010106.

[16] D. Tomus, Y. Tian, P.A. Rometsch, M. Heilmaier, X. Wu, Influence of post heat treatments on anisotropy of mechanical behaviour and microstructure of Hastelloy-X parts produced by selective laser melting, Mater. Sci. Eng. A. 667 (2016) 42–53. doi:10.1016/j.msea.2016.04.086.

[17] Q. Han, R. Mertens, M. Montero-Sistiaga, S. Yang, R. Setchi, K. Vanmeensel, B. Hooreweder, S.L. Evans, H. Fan, Laser powder bed fusion of Hastelloy X: effects of hot isostatic pressing and the hot cracking mechanism, Mater. Sci. Eng. A. 732 (2018) 228–239. doi:https://doi.org/10.1016/j.msea.2018.07.008.

[18] M.L. Montero-Sistiaga, S. Pourbabak, J. Van Humbeeck, D. Schryvers, K. Vanmeensel, Microstructure and mechanical properties of Hastelloy X produced by HP-SLM (high power selective laser melting), Mater. Des. 105 (2019) 107598. doi:10.1016/j.matdes.2019.107598.

[19] A. Keshavarzkermani, E. Marzbanrad, R. Esmaeilizadeh, Y. Mahmoodkhani, U. Ali, P.D. Enrique, N.Y. Zhou, A. Bonakdar, E. Toyserkani, An investigation into the effect of process parameters on melt pool geometry, cell spacing, and grain refinement during laser powder bed fusion, Opt. Laser Technol. 116 (2019) 83–91. doi:10.1016/j.optlastec.2019.03.012.

[20] H. Brodin, O. Andersson, S. Johansson, Mechanical behaviour and microstructure correlation in a selective laser melted superalloy, in: Proc. ASME Turbo Expo, 2013. doi:10.1115/GT2013-95878.

[21] C. De Formanoir, S. Michotte, O. Rigo, L. Germain, S. Godet, Electron beam melted Ti-6Al-4V: Microstructure, texture and mechanical behavior of the as-built and heat-treated material, Mater. Sci. Eng. A. 652 (2016) 105–119. doi:10.1016/j.msea.2015.11.052.

[22] P.C. Collins, D.A. Brice, P. Samimi, I. Ghamarian, H.L. Fraser, Microstructural Control of Additively Manufactured Metallic Materials, Annu. Rev. Mater. Res. 46 (2016) 1–18. doi:10.1146/annurev-matsci-070115-031816.

[23] M.M. Kirka, P. Nandwana, Y. Lee, R.R. Dehoff, Solidification and solid-state transformation sciences in metals additive manufacturing, Scr. Mater. 135 (2017) 130–134.

doi:10.1016/j.scriptamat.2017.01.005.

[24] Q. Han, Y. Jiao, Effect of heat treatment and laser surface remelting on AlSi10Mg alloy fabricated by selective laser melting, Int. J. Adv. Manuf. Technol. 102 (2019) 3315–3324. doi:10.1007/s00170-018-03272-y.

[25] O. Sanchez-Mata, X. Wang, J.A. Muñiz-Lerma, M.A. Shandiz, R. Gauvin, M. Brochu, Fabrication of crack-free nickel-based superalloy considered non-weldable during laser powder bed fusion, Materials (Basel). 11 (2018) 1288. doi:10.3390/ma11081288.

[26] J.H. Martin, B.D. Yahata, J.M. Hundley, J.A. Mayer, T.A. Schaedler, T.M. Pollock, 3D printing of high-strength aluminium alloys, Nature. 549 (2017) 365–369. doi:10.1038/nature23894.

[27] C. Hong, D. Gu, D. Dai, M. Alkhayat, W. Urban, P. Yuan, S. Cao, A. Gasser, A. Weisheit, I. Kelbassa, M. Zhong, R. Poprawe, Laser additive manufacturing of ultrafine TiC particle reinforced Inconel 625 based composite parts: Tailored microstructures and enhanced performance, Mater. Sci. Eng. A. (2015). doi:10.1016/j.msea.2015.03.043.

[28] B. Zheng, T. Topping, J.E. Smugeresky, Y. Zhou, A. Biswas, D. Baker, E.J. Lavernia, The influence of Ni-coated TiC on laser-deposited IN625 metal matrix composites, Metall. Mater. Trans. A Phys. Metall. Mater. Sci. (2010). doi:10.1007/s11661-009-0126-5.

[29] D. Turnbull, B. Vonnegut, Nucleation Catalysis., Ind. Eng. Chem. 44 (1952) 1292–1298. doi:10.1021/ie50510a031.

[30] B.L. Bramfitt, The effect of carbide and nitride additions on the heterogeneous nucleation behavior of liquid iron, Metall. Trans. 1 (1970) 1987–1995. doi:10.1007/BF02642799.

[31] Standard Test Methods for Tension Testing of Metallic Materials, (n.d.). https://compass.astm.org/Standards/HISTORICAL/E8E8M-13A.htm (accessed September 15, 2018).

[32] K. Guan, Z. Wang, M. Gao, X. Li, X. Zeng, Effects of processing parameters on tensile properties of selective laser melted 304 stainless steel, Mater. Des. 50 (2013) 581–586. doi:10.1016/j.matdes.2013.03.056.

[33] C. Qiu, N.J.E. Adkins, M.M. Attallah, Selective laser melting of Invar 36: Microstructure and properties, Acta Mater. (2016). doi:10.1016/j.actamat.2015.10.020.

[34] Q. Han, R. Setchi, S.L. Evans, Synthesis and characterisation of advanced ball-milled Al-Al2O3 nanocomposites for selective laser melting, Powder Technol. 297 (2016) 183–192. doi:10.1016/j.powtec.2016.04.015.

[35] J. Zhang, R.F. Singer, Effect of Grain-Boundary Characteristics on Castability of Nickel-Base Superalloys, Metall. Mater. Trans. A Phys. Metall. Mater. Sci. 35 (2004) 939–946. doi:10.1007/s11661-004-0018-7.

[36] Y.Z. Zhou, A. Volek, Effect of grain boundary fraction on castability of a directionally solidified nickel alloy, Scr. Mater. 12 (2006) 2169–2174. doi:10.1016/j.scriptamat.2006.02.032.

[37] Y.M. Wang, T. Voisin, J.T. McKeown, J. Ye, N.P. Calta, Z. Li, Z. Zeng, Y. Zhang, W. Chen, T.T. Roehling, R.T. Ott, M.K. Santala, P.J. Depond, M.J. Matthews, A. V. Hamza, T. Zhu, Additively manufactured hierarchical stainless steels with high strength and ductility, Nat. Mater. 17 (2018) 63. doi:10.1038/NMAT5021.

[38] R. Acharya, J.A. Sharon, A. Staroselsky, Prediction of microstructure in laser powder bed fusion process, Acta Mater. 124 (2017) 360–371. doi:10.1016/j.actamat.2016.11.018.

[39] X.P. Li, X.J. Wang, M. Saunders, A. Suvorova, L.C. Zhang, Y.J. Liu, M.H. Fang, Z.H. Huang, T.B. Sercombe, A selective laser melting and solution heat treatment refined Al-12Si alloy with a controllable ultrafine eutectic microstructure and 25% tensile ductility, Acta Mater. 95 (2015) 74–82. doi:10.1016/j.actamat.2015.05.017.

[40] C.L.A. Leung, S. Marussi, R.C. Atwood, M. Towrie, P.J. Withers, P.D. Lee, In situ X-ray imaging of defect and molten pool dynamics in laser additive manufacturing, Nat. Commun.

(2018). doi:10.1038/s41467-018-03734-7.

[41] C. Qiu, C. Panwisawas, M. Ward, H.C. Basoalto, J.W. Brooks, M.M. Attallah, On the role of melt flow into the surface structure and porosity development during selective laser melting, Acta Mater. 96 (2015) 72–79. doi:10.1016/j.actamat.2015.06.004.

[42] M. Ma, Z. Wang, X. Zeng, A comparison on metallurgical behaviors of 316L stainless steel by selective laser melting and laser cladding deposition, Mater. Sci. Eng. A. 685 (2017) 265–273. doi:10.1016/j.msea.2016.12.112.

[43] A.B. Spierings, K. Dawson, T. Heeling, P.J. Uggowitzer, R. Schäublin, F. Palm, K. Wegener, Microstructural features of Sc- and Zr-modified Al-Mg alloys processed by selective laser melting, Mater. Des. 115 (2017) 52–63. doi:10.1016/j.matdes.2016.11.040.

[44] E. Chlebus, K. Gruber, B. Kuźnicka, J. Kurzac, T. Kurzynowski, Effect of heat treatment on the microstructure and mechanical properties of Inconel 718 processed by selective laser melting, Mater. Sci. Eng. A. 639 (2015) 647–655. doi:10.1016/j.msea.2015.05.035.

[45] K.G. Prashanth, J. Eckert, Formation of metastable cellular microstructures in selective laser melted alloys, J. Alloys Compd. 707 (2017) 27–34. doi:10.1016/j.jallcom.2016.12.209.

[46] P. Vora, K. Mumtaz, I. Todd, N. Hopkinson, AlSi12 in-situ alloy formation and residual stress reduction using anchorless selective laser melting, Addit. Manuf. 7 (2015) 12–19. doi:10.1016/j.addma.2015.06.003.

[47] P. Mercelis, J. Kruth, Residual stresses in selective laser sintering and selective laser melting, Rapid Prototyp. J. 12 (2006) 254–265. doi:10.1108/13552540610707013.